Macroscopic quantum entanglement between an optomechanical cavity and a continuous field in presence of non-Markovian noise

S. Direkci [1,*] K. Winkler [2] C. Gut,[2] K. Hammerer [3] M. Aspelmeyer,[4,5] and Y. Chen[1]

[1] *Theoretical Astrophysics 350-17, California Institute of Technology, Pasadena, California 91125, USA*

[2] *Vienna Center for Quantum Science and Technology (VCQ), Faculty of Physics & Vienna Doctoral School in Physics, University of Vienna, A-1090 Vienna, Austria*

[3] *Institute for Theoretical Physics and Institute for Gravitational Physics (Albert-Einstein-Institute), Leibniz University Hannover, Appelstrasse 2, 30167 Hannover, Germany*

[4] *Vienna Center for Quantum Science and Technology (VCQ), Faculty of Physics, University of Vienna, A-1090 Vienna, Austria*

[5] *Institute for Quantum Optics and Quantum Information (IQOQI) Vienna, Austrian Academy of Sciences, Boltzmanngasse 3, 1090 Vienna, Austria*

(Received 21 September 2023; accepted 23 January 2024; published 16 February 2024)

Probing quantum entanglement with macroscopic objects allows us to test quantum mechanics in new regimes. One way to realize such behavior is to couple a macroscopic mechanical oscillator to a continuous light field via radiation pressure. In view of this, the system that is discussed comprises an optomechanical cavity driven by a coherent optical field in the unresolved sideband regime where we assume Gaussian states and dynamics. We develop a framework to quantify the amount of entanglement in the system numerically. Different from previous work, we treat non-Markovian noise and take into account both the continuous optical field and the cavity mode. We apply our framework to the case of the Advanced Laser Interferometer Gravitational-Wave Observatory and discuss the parameter regimes where entanglement exists, even in the presence of quantum and classical noises.

DOI: 10.1103/PhysRevResearch.6.013175

I. INTRODUCTION

Entanglement is one of the hallmarks of the "quantumness" of physical systems. Ideally, it is possible for macroscopic objects, massive and/or containing a high number of degrees of freedom, to be entangled with each other. Yet in practice, such macroscopic entanglement can be very delicate in the presence of decoherence. It is an intriguing challenge to create and verify macroscopic entanglement, which is often viewed as expanding the limits of the quantum regime.

Optomechanical systems are promising candidates for experimental demonstration of macroscopic entanglement, partly due to their theoretical robustness against mechanical decoherence imposed by coupling to a possibly highly populated thermal bath [1]. They can also be used to engineer the quantum state of the mechanical system [2], where the entanglement is generated by the momentum exchange between the light reflecting from the mechanical oscillator—a phenomenon known as radiation pressure. It is theoretically well understood and broadly discussed in the literature [3–8]; see, for example, Refs. [1,9] for a review.

Entanglement in optomechanical devices has been widely studied, and there have been several successful experimental realizations: stationary entanglement between simultaneous light tones mediated by an optomechanical device [10,11], generation of entanglement between spaced mechanical oscillators both in the micro and macro regime via radiation pressure [12–15], and optomechanical entanglement between the light field and the mechanical oscillator in a pulsed scheme [16] are examples of such demonstrations. There also exist many proposals in the literature to further study macroscopic quantum phenomena in optomechanical systems [17–21] and entanglement between coupled oscillators in the presence of non-Markovian baths [22]. In this work, we consider stationary optomechanical entanglement, where the system parameters (e.g., the driving), and statistical behavior thereof, are not changing over time. Schemes to verify stationary optomechanical entanglement were proposed in [4,6,23–25], whereas to the best of our knowledge an experimental demonstration has not been performed yet.

Our system consists of a single mechanical mode interacting with an optical cavity mode and the quadratures of the light field exiting the cavity. At any time t, we study the bipartite entanglement that is present in the joint quantum state between mechanical mode, optical mode, and the light that has exited the system during $t' \leqslant t$. See Fig. 1 of Ref. [6], which includes a space-time diagram that illustrates the configuration. In the regime where the dynamics are linear, the state is Gaussian, and the noise processes are Markovian (white), the open-system optomechanical dynamics is solvable analytically, and the state of the system can be known

*sdirekci@caltech.edu

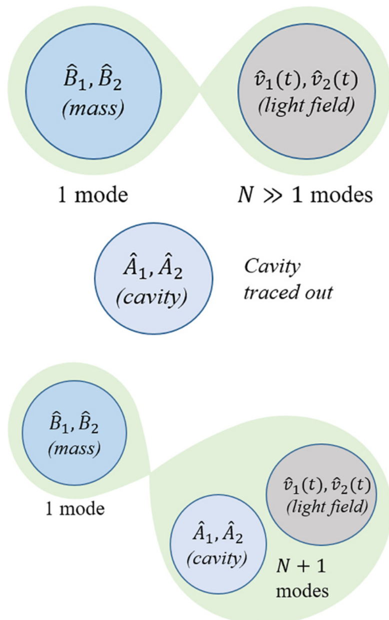

FIG. 1. Figurative representation of the two different partitions that is used while testing for entanglement, which are partitioning by tracing over (top row) and *not* tracing over (bottom row) the cavity. Note that the system configuration is not changed, i.e., the cavity is still present for both partitions.

exactly [3]. The white-noise model describes well devices with high-frequency oscillators, where only thermal excitations are expected, and in the limit of large bath temperature where $k_B T \gg \hbar\omega_m$, T is the temperature of the bath and ω_m is the resonance frequency of the oscillator [26].

In this work, we extend the description to non-Markovian Gaussian noise processes where analytical results are, to our knowledge, not available, thus requiring numerical methods. This approach is applicable whenever non-white-noise processes, such as structural damping [27–30], are relevant. We extend the methods developed in [6], incorporating a cavity, and, more importantly, non-Markovian noise processes. The technique consists in computing the minimal symplectic eigenvalue of the partially transposed covariance matrix of the system, constructed with numerical methods, which provides a measure of appropriate bipartite entanglement.

We first investigate entanglement in a generalized setting, considering a heavy suspended oscillator with a low mechanical resonance frequency. This corresponds to the free-mass limit, where the mechanical resonance frequency is much smaller than the other characteristic frequencies of the system. We work in this limit to study the general behavior of heavy suspended oscillators affected by environmental decoherence, however the algorithm does not require this assumption. Subsequently, we stop working in the free-mass limit and focus our attention on the Advanced Laser Interferometer Gravitational-Wave Observatory (aLIGO), [31] using it as a case study. It has been recently shown that by injecting squeezed vacuum, the detector's quantum noise can in principle surpass the free-mass standard quantum limit (SQL) by 3 dB [32]. It is natural to ask whether this can already imply that aLIGO has built quantum entanglement between the mirrors and the light field. The answer to this question is nontrivial. First, from [32], we see that the level of classical noise is not yet below the SQL [33]. Second, the strict definition of entanglement we use here requires integrating over all frequencies: it remains uncertain whether having noise below the SQL within a certain finite frequency band automatically leads to entanglement. Therefore, we parametrize aLIGO's noise curves to investigate regimes where entanglement, according to its strict definition, exists.

This paper is organized as follows: In Sec. II, we introduce the dynamics of the system and its equations of motion. In Sec. III, we state our entanglement criterion and the covariance matrix of the system for two partitions of interest. To show the usefulness of our technique for systems with low mechanical resonance frequencies, we investigate entanglement in a generalized setting in Sec. IV. In Sec. V, we give details about aLIGO's noise budget, and talk about how we model it in our calculations. Finally, in Sec. VI, we investigate whether there is entanglement between the mechanical oscillator and the light field at aLIGO for the partitions of interest, given different parametrizations of the classical noise curves.

II. SYSTEM DYNAMICS

Let us consider an optical cavity with a movable mirror, driven by a laser with frequency ω_0 close to one of the resonant frequencies of the cavity, $\omega_0 + \Delta$ [34]. The quantity Δ is often referred to as the detuning frequency of the cavity. For such a system, the linearized Hamiltonian in the interaction picture with the rotating-wave approximation (RWA) is given by [35]

$$\begin{aligned} H &= \hbar\omega_m \hat{B}^\dagger \hat{B} + \hbar\Delta \hat{A}^\dagger \hat{A} - \hbar G \hat{x}(\hat{A}^\dagger + \hat{A}) \\ &\quad + i\hbar\sqrt{2\gamma}\int_{-\infty}^{\infty} \frac{d\Omega}{2\pi}[\hat{A}^\dagger \hat{c}(\omega_0+\Omega) - \hat{A}\hat{c}^\dagger(\omega_0+\Omega)] \\ &\quad + \int_{-\infty}^{\infty} \frac{d\Omega}{2\pi}[\hbar\Omega \hat{c}^\dagger(\omega_0+\Omega)\hat{c}(\omega_0+\Omega)], \end{aligned} \tag{1}$$

where $\hat{B}$ and $\hat{B}^\dagger$ are the annihilation and creation operators of the mechanical mode (center-of-mass motion of the mirror), $\hat{x}$ is the position of the center of mass of the mirror, ω_m is the mechanical resonance frequency, $\hat{A}$ and $\hat{A}^\dagger$ are the annihilation and creation operators of the cavity mode, $\hat{c}(\omega_0 + \Omega)$ and $\hat{c}^\dagger(\omega_0 + \Omega)$ are the annihilation and creation operators of the external vacuum light field at frequency $\omega_0 + \Omega$, G is the linear optomechanical coupling constant, and γ is the decay rate of the cavity mode. The position and momentum operators of the mirror are related to the creation and annihilation operators of the mechanical mode by

$$\hat{x} = \sqrt{\frac{\hbar}{M\omega_m}}\frac{(\hat{B} + \hat{B}^\dagger)}{\sqrt{2}}, \tag{2a}$$

$$\hat{p} = \sqrt{\hbar M\omega_m}\frac{(\hat{B} - \hat{B}^\dagger)}{\sqrt{2}i}. \tag{2b}$$

Note that for the sake of convenience, we chose a displaced frame where all operators have zero mean. The mode operators satisfy the canonical commutation relations,

$$[\hat{A}, \hat{A}^\dagger] = [\hat{B}, \hat{B}^\dagger] = 1. \tag{3}$$

aLIGO detectors are power- and signal-recycled Fabry-Pérot Michelson interferometers, which contain a high number of degrees of freedom. However, the core optomechanics can still be studied by the Hamiltonian given above; this reduction manifests itself in the "scaling-law" relations governing aLIGO's sensitivity as parameters of the signal-recycling cavity are modified [34]. From the scaling-law, the coupling constant G is related to the parameters of the interferometer by

$$G = \sqrt{\frac{2\omega_0 P_c}{\hbar L c}}, \quad (4)$$

where L is the arm length of the interferometer (i.e., the cavity length), P_c is the power circulating inside the cavity, and c is the speed of light in vacuum.

We can transform the Hamiltonian such that the cavity mode $(A, A^\dagger)$ couples with the traveling wave at $z = 0$ (where the pointwise cavity interface is located). We derive this transformation in Appendix A. We use $\hat{u}$ and $\hat{v}$ to label the field right before entering and right after exiting the cavity, respectively.

In this paper, we restrict ourselves to $\Delta = 0$. In this resonant case, the system is unconditionally stable and it reaches a steady state, in which the Heisenberg equations can be solved using Fourier transformation [36]. To write down and solve the Heisenberg equations, instead of annihilation and creation operators we use the Caves-Schumaker quadrature operators [37,38]:

$$\hat{u}_1(\Omega) = \frac{\hat{u}(\omega_0 + \Omega) + \hat{u}^\dagger(\omega_0 - \Omega)}{\sqrt{2}}, \quad (5a)$$

$$\hat{u}_2(\Omega) = \frac{\hat{u}(\omega_0 + \Omega) - \hat{u}^\dagger(\omega_0 - \Omega)}{\sqrt{2}i}, \quad (5b)$$

where $\hat{u}_j^\dagger(\Omega) = \hat{u}_j(-\Omega)$. Quadratures $\hat{v}_1(\Omega)$ and $\hat{v}_2(\Omega)$ are defined from $\hat{v}(\omega_0 + \Omega)$ and $\hat{v}(\omega_0 - \Omega)$ in a similar fashion. Their commutation relations are [39]

$$[\hat{u}_1(\Omega), \hat{u}_2(\Omega')] = [\hat{v}_1(\Omega), \hat{v}_2(\Omega')] = 2\pi\delta(\Omega + \Omega'), \quad (6a)$$

$$[\hat{u}_j(\Omega), \hat{u}_j(\Omega')] = [\hat{v}_j(\Omega), \hat{v}_j(\Omega')] = 0 \quad (6b)$$

for $j = 1, 2$. Then, in the time domain, we have

$$\hat{u}_j(t) = \int_{-\infty}^{\infty} \frac{d\Omega}{2\pi} \hat{u}_j(\Omega) e^{-i\Omega t}, \quad (7a)$$

$$[\hat{u}_1(t), \hat{u}_2(t')] = i\delta(t - t'), \quad (7b)$$

$$[\hat{u}_1(t), \hat{u}_1(t')] = [\hat{u}_2(t), \hat{u}_2(t')] = 0 \quad (7c)$$

for $j = 1, 2$. We similarly define quadrature operators $\hat{A}_{1,2}$ and $\hat{B}_{1,2}$, in the *time domain*, with

$$\hat{A}_1(t) = \frac{\hat{A}(t) + \hat{A}^\dagger(t)}{\sqrt{2}}, \quad \hat{A}_2(t) = \frac{\hat{A}(t) - \hat{A}^\dagger(t)}{\sqrt{2}i}, \quad (8)$$

and similarly for $\hat{B}_{1,2}$. We also have

$$[\hat{A}_1(t), \hat{A}_1(t)] = [\hat{A}_2(t), \hat{A}_2(t)] = 0, \quad (9)$$

$$[\hat{A}_1(t), \hat{A}_2(t)] = i, \quad (10)$$

and the same for $\hat{B}_{1,2}$. Note here that the commutators are for same-time operators.

We include two classes of "classical" noises [39] in our system: a force noise $\hat{n}_F$ and a sensing noise $\hat{n}_X$, originally arising from a quantum treatment of the interaction of the system with its environment. We label them as "classical" noises because we assume that the details—and possible quantum limit—of a microscopic model of these noises are irrelevant (typically because they arise from thermal baths in the high-temperature limit) unlike the noise arising from vacuum fluctuations, $\hat{u}_1(\Omega)$ and $\hat{u}_2(\Omega)$. Force noise affects the center-of-mass motion of the mechanical oscillator by introducing fluctuations in its momentum. We also introduce a velocity damping of the oscillator, with a damping rate γ_m. γ_m and n_F are associated with the heat bath(s) the mass is coupled to, with the value of γ_m and the spectrum of n_F related by the fluctuation-dissipation theorem [40]. Sensing noise affects how the position is measured by the light field. In our model below it arises from fluctuations of the reflecting surface that introduces noise in the cavity field.

In the Heisenberg picture, the dynamics are given by the Langevin equations of motion. In the Fourier domain, they are written as

$$-i\Omega\hat{A}_1 = -\gamma\hat{A}_1 + \sqrt{2\gamma}\hat{u}_1, \quad (11a)$$

$$-i\Omega\hat{A}_2 = -\gamma\hat{A}_2 + \sqrt{2\gamma}\hat{u}_2 + \sqrt{2}G(\hat{x} + \hat{n}_X), \quad (11b)$$

$$-i\Omega\hat{x} = \hat{p}/M, \quad (11c)$$

$$-i\Omega\hat{p} = -\gamma_m\hat{p} - M\omega_m^2\hat{x} + \sqrt{2}\hbar G\hat{A}_1 + \hat{n}_F, \quad (11d)$$

$$\hat{v}_1 = \hat{u}_1 - \sqrt{2\gamma}\hat{A}_1, \quad (11e)$$

$$\hat{v}_2 = \hat{u}_2 - \sqrt{2\gamma}\hat{A}_2. \quad (11f)$$

We refer to Eqs. (11) as the Heisenberg equations for the rest of the article. It is straightforward to solve them to obtain $(\hat{x}, \hat{p}, \hat{A}_{1,2}, \hat{v}_{1,2})$ in terms of the input fields, $(\hat{u}_{1,2}, \hat{n}_X, \hat{n}_F)$, referred to as the input-output relations of the system. More specifically, quantum fluctuations in the ingoing quadratures $\hat{u}_{1,2}(\Omega)$ drive the system's quantum noise [41]. From Eqs. (11e) and (11f), reading the outgoing field quadratures are subject to noises in $\hat{u}_1$ and $\hat{u}_2$, giving rise to the *shot noise* (SN) for that readout strategy [41]. On the other hand, from Eq. (11a), we see that $\hat{u}_1$ drives $\hat{A}_1$, which in Eq. (11d) drives the momentum of the test mass, which then shows up in the position of the test mass via Eq. (11c), giving rise to *quantum radiation pressure noise* (QRPN), also known as backaction noise in the literature. In general, the power spectrum of the SN is inversely proportional to circulating power in the cavity, while that of the QRPN is proportional to circulating power.

III. ENTANGLEMENT CRITERIA AND PARTITIONS

The canonical commutation relations imply that $\mathbf{V} + \frac{1}{2}\mathbf{K}$ is positive-semidefinite, where $\mathbf{V}$ is the covariance matrix with $\mathbf{V}_{ij} = \langle\{\hat{X}_i - \langle\hat{X}_i\rangle, \hat{X}_j - \langle\hat{X}_j\rangle\}\rangle/2$, and $\mathbf{K}_{ij} = [\hat{X}_i, \hat{X}_j]$ is the commutator matrix of the quadratures in the system. This relation can be stated as

$$\mathbf{V} + \tfrac{1}{2}\mathbf{K} \geqslant 0. \quad (12)$$

Here for an N-partite system containing N harmonic oscillators, the matrices $\mathbf{V}$ and $\mathbf{K}$ are $2N$-dimensional.

To test for bipartite entanglement in a multimode system, we use the positivity of the partial transpose (PPT) criterion, which is necessary and sufficient to test for the separability of one of the modes from the rest for Gaussian systems [42–44]. To use the PPT criterion in this context, one obtains the partial-transposed covariance matrix $\mathbf{V}_{\rm pt}$ by reverting the momentum of that one mode (which puts a minus sign on the column and the row that contains the momentum in question) [45]. The PPT criterion for separability is expressed as

$$\mathbf{V}_{\rm pt} + \tfrac{1}{2}\mathbf{K} \geqslant 0 \Leftrightarrow \text{Separability}. \tag{13}$$

The amount of entanglement is quantified by the logarithmic negativity, $E_{\mathcal{N}}$ [46]. For a Gaussian state of N modes, it is defined as

$$E_{\mathcal{N}} = \sum_{j=1}^{N} \max\{0, -\log_2(\tilde{\nu}_j)\}, \tag{14}$$

where $\tilde{\nu}_j$, $j = 1, \dots, N$ are the symplectic eigenvalues of the partially transposed covariance matrix, $\mathbf{V}_{\rm pt}$, which are given by the absolute values of the eigenvalues of $\mathbf{K}^{-1}\mathbf{V}_{\rm pt}$. For 1 versus $N-1$ mode partitions, only one of the symplectic eigenvalues of $\mathbf{V}_{\rm pt}$ can have a magnitude smaller than 1 [47], therefore there can be at most one negative eigenvalue of $\mathbf{V}_{\rm pt} + \frac{1}{2}\mathbf{K}$. We label the corresponding symplectic eigenvalue as $\tilde{\nu}_{\rm min}$.

Using the PPT criterion, we test for entanglement between the mechanical oscillator and the optical field in two ways: first, we construct the covariance matrix $\mathbf{V}$ with the mechanical mode and the modes of the light field, essentially tracing out the cavity mode. Here, we perform the partial transpose operation with respect to the mechanical oscillator. Second, we include the cavity mode in the covariance matrix while still taking the partial transpose with respect to the mechanical oscillator, which corresponds to measuring the entanglement between the oscillator and the joint system of the cavity plus external light field. The two ways of partitioning are depicted in Fig. 1. The elements of the covariance matrix $\mathbf{V}$ for both types of partitions, as well as the discretization of $\mathbf{V}$, can be found in Appendix D.

IV. ENTANGLEMENT IN THE PRESENCE OF NON-MARKOVIAN NOISES

Due to the numerical nature of the algorithm, we can tackle any noise spectral density associated with $\hat{u}_1(\Omega)$, $\hat{u}_2(\Omega)$, $\hat{n}_F(\Omega)$, and $\hat{n}_X(\Omega)$ using the PPT criterion defined in Eq. (13) to determine whether entanglement is present for a given partition. Conversely, this problem is analytically solvable only for some simplified noise models to our knowledge, such as assuming all the noise sources to have a white spectrum [6,23].

To show the usefulness of the method, we investigate entanglement in heavy suspended oscillators with relatively low mechanical resonance frequencies. Examples of such systems are aLIGO, KAGRA [48], and VIRGO [49], but also smaller devices such as those in [50,51]. For such systems, the mechanical resonance frequency, ω_m, is much smaller than the other frequencies of the system, which is referred to as the *free-mass limit*. In this setting, ω_m essentially does not affect the dynamics. Furthermore, in this limit where $\Omega \gg \omega_m, \gamma_m$, the tradeoff between shot noise and QRPN gives rise to the SQL [52], given by

$$S_{\rm SQL}(\Omega) = \frac{2\hbar}{M\Omega^2}. \tag{15}$$

In the context of suspended oscillators, $\hat{n}_F(\Omega)$ is the force that gives rise to the suspension thermal noise, whereas $\hat{n}_X(\Omega)$ is an effective displacement that gives rise to coating thermal noise. When thermal noise is due to the internal friction of the suspension or the oscillator, the noise spectrum of $\hat{n}_F(\Omega)$ and $\hat{n}_X(\Omega)$ decreases as $1/\Omega$ above internal resonances, which is referred to as *structural damping* [27,28,53]. Evidently, structural damping gives rise to non-Markovian noises, and the position-referred noise spectral densities of $\hat{n}_F(\Omega)$ and $\hat{n}_X(\Omega)$ are given, in the free-mass limit, by

$$S_F(\Omega) = \frac{2\hbar}{M}\frac{\Omega_F^3}{|\Omega|^5}, \tag{16a}$$

$$S_X(\Omega) = \frac{2\hbar}{M}\frac{1}{\Omega_X|\Omega|}, \tag{16b}$$

where Ω_F and Ω_X are the frequencies where the respective noise curves cross the SQL, given in Eq. (15). Accordingly, they encode the strength of the noise processes n_F and n_X, relative to the SQL level. For $\hat{n}_F(\Omega)$, the position-referred spectrum is related to the noise spectral density, labeled as $S_{n_F}(\Omega)$, with $S_F(\Omega) = S_{n_F}(\Omega)/M^2\Omega^4$, whereas for $\hat{n}_X(\Omega)$, the position-referred spectrum $S_X(\Omega)$ is also the noise spectral density $S_{n_X}(\Omega)$ [54]. The incoming field quadratures $\hat{u}_j$ have uncorrelated white spectra given by Eq. (D8), since we assume the incoming field to be at vacuum state.

In the limit of a large cavity bandwidth, $\gamma \gg \Omega$, the cavity can be eliminated adiabatically. Then, the equations of motion in (11) are modified as

$$\hat{v}_1(\Omega) = \hat{u}_1(\Omega), \tag{17a}$$

$$\hat{v}_2(\Omega) = \hat{u}_2(\Omega) + \alpha(\hat{x}(\Omega) + \hat{n}_X(\Omega)), \tag{17b}$$

$$-i\Omega\hat{p}(\Omega) = -\gamma_m\hat{p}(\Omega) - M\omega_m^2\hat{x}(\Omega) + \hbar\alpha\hat{u}_1(\Omega) + \hat{n}_F(\Omega), \tag{17c}$$

$$-i\Omega\hat{x}(\Omega) = \hat{p}(\Omega)/M, \tag{17d}$$

where $\alpha = \Omega_q\sqrt{M/\hbar}$, and $\Omega_q = 2G\sqrt{\hbar/M\gamma}$ is the characteristic interaction frequency. In the context of structural damping, there is no velocity damping, Instead, the damping arises from a complex spring constant associated with the mechanical oscillator. Accordingly, Eq. (17b) is modified as

$$-i\Omega\hat{p}(\Omega) = -M\omega_m^2(1 + i\,\phi(\Omega))\hat{x}(\Omega) + \hbar\alpha\hat{u}_1(\Omega) + \hat{n}_F(\Omega), \tag{18}$$

where $\phi(\Omega)$ is referred to as the *loss angle*. When structural damping is present, $\phi(\Omega)$ is constant for a large band of frequencies and goes to zero as $\Omega \to 0$, however the dependence of $\phi(\Omega)$ to Ω depends on the properties of the material [27]. Numerically, we choose to model this with $\phi(\Omega) = \phi\Omega/(\Omega + \Omega_c)$, so that $\phi(\Omega) \approx \phi$ for $\Omega \gg \Omega_c$ and $\phi(0) = 0$ for some cutoff frequency Ω_c. Then, Ω_c determines the noise power of $\hat{n}_F$ and $\hat{n}_X$ at 0 Hz.

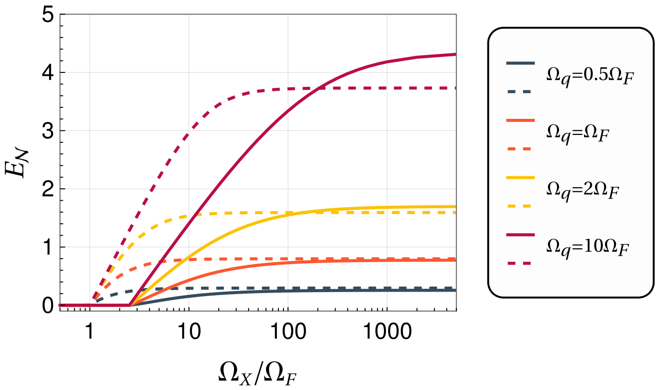

FIG. 2. Logarithmic negativity between the mechanical oscillator and the outgoing light field in the free mass limit as a function of Ω_X/Ω_F for various Ω_q/Ω_F. We plot the results for Markovian and non-Markovian force and sensing noise with dashed and plain lines, respectively. Note that entanglement does not exist for $\Omega_X/\Omega_F \lesssim 1$ with Markovian and for $\Omega_X/\Omega_F \lesssim 2.6$ with non-Markovian noise sources, for $\omega_m/(2\pi) = 1$ Hz, $\gamma_m/(2\pi) = 0.01$ Hz, $\phi = 0.05$, and a cutoff frequency of $\Omega_c/(2\pi) = 0.05$ Hz.

We fix $\omega_m/(2\pi) = 1$ Hz, $\Omega_F/(2\pi) = 100$ Hz, $\Omega_c/(2\pi) = 0.05$ Hz, and $\phi = 0.05$, and we vary Ω_X and Ω_q. Note that the aim of these choices is to ensure that $\Omega_F \gg \omega_m$, i.e., that the free-mass limit is justified. This choice also implies the large bath temperature limit where $k_B T \gg \hbar\omega_m$, T being the temperature of the bath. Furthermore, $\Omega_q \gg \omega_m$ ensures that the measurement of the system performed by light is faster than the dynamics of the system. Lastly, we perform the simulations by sampling the covariance matrix for $\tau = 0.1$ s, from $t = -0.1$ to 0 s, where t indicates the time (for the sampling of the covariance matrix; see Appendix D). Hence, we cannot resolve the very low frequency regime of Ω_c. Physically, this corresponds to the finite detection frequency resolution that renders the behavior of ϕ at the cutoff inaccessible. In this sense, one might expect Ω_c to be irrelevant. However, we see that it does affect the final characterization of entanglement, due to its contribution to the total variance of the quadratures of the mechanical oscillator.

After specifying the low-frequency behavior of ϕ with Ω_c, the relevant parameters on which the presence of entanglement depends are Ω_q, Ω_F, and Ω_X. Then, working in the free-mass limit enables us to examine the general behavior of suspended oscillators with low mechanical resonance frequencies, classified by their coating materials and suspension systems (i.e., the low-frequency behavior of ϕ). Therefore, we look for entanglement between the oscillator and the outgoing light field by varying the ratio Ω_X/Ω_F for various Ω_q in Fig. 2, and we plot the results with plain lines. We find that for $\Omega_c/(2\pi) = 0.05$ Hz, entanglement does not exist for $\Omega_X/\Omega_F \lesssim 2.6$ for any value of Ω_q. For $\Omega_X/\Omega_F \gtrsim 2.6$, the system is entangled for any (finite) Ω_q, and the entanglement increases monotonously with increasing Ω_X/Ω_F. This implies the existence of "universal" entanglement, meaning that whether the system is entangled or not is independent of Ω_q, the interaction frequency (or, in other words, how fast the system is measured by light). When the system is entangled, the amount of entanglement increases when Ω_q is increased.

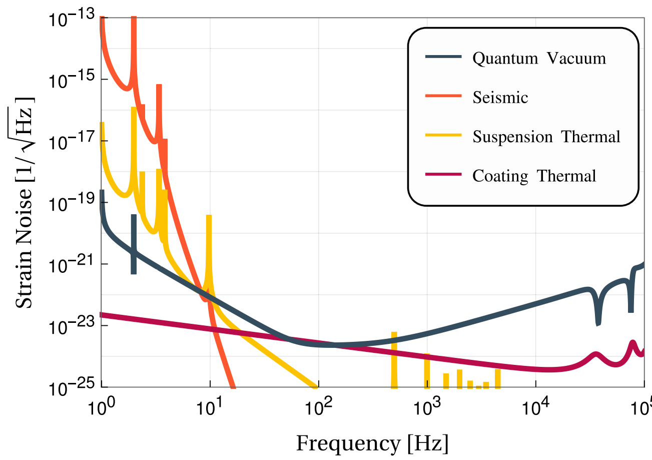

FIG. 3. aLIGO noise budget obtained from pygwinc. Only the dominant classical noise sources are plotted, along with the quantum noise. The total force noise in the system is the sum of the seismic noise and the suspension thermal noise, which is effective at low frequencies. The coating Brownian thermal noise is taken as the main constituent of the sensing noise. As can be seen from the figure, quantum noise dominates over the sensing noise by a large margin at high frequencies.

We also note that the threshold for Ω_X/Ω_F above which the system is entangled depends on the low-frequency cutoff Ω_c chosen in our model for the spectra of $\hat{n}_F$ and $\hat{n}_X$. We saw that the threshold is inversely proportional to the cutoff frequency.

To see the significance of non-Markovianity on the results, we repeat the same procedure with a white force and sensing noise. The noise spectra are given by $S_{n_F}(\Omega) = 2\hbar M\Omega_F^2$, $S_F(\Omega) = 2\hbar\Omega_F^2/M\Omega^4$, and $S_{n_X}(\Omega) = S_X(\Omega) = 2\hbar/M\Omega_X^2$. The results can again be found in Fig. 2, plotted with dashed lines, where the system is not entangled for any Ω_q when $\Omega_X/\Omega_F \lesssim 1$, whereas for $\Omega_X/\Omega_F \gtrsim 1$, entanglement exists for all Ω_q and the amount of entanglement increases with increasing Ω_q. Since we see this behavior for both Markovian and non-Markovian noise, we prove that the universality of the entangling-disentangling phase transition is independent of the power spectral densities of the classical noises, and that the power spectral densities only determine the threshold above which we have entanglement for all Ω_q in a manuscript that is currently in preparation.

V. NOISE MODEL OF aLIGO

The primary noise sources in aLIGO, other than the quantum noise, are the following [31]: seismic noise and suspension thermal noise are the main constituents of the force noise, and mirror coating thermal noise constitutes the sensing noise. The noise spectrum is dominated by seismic and thermal noise at low frequencies (until 100 Hz), and quantum noise at high frequencies, cf. Fig. 3. The interferometer noise is stationary and Gaussian to very good approximation in the absence of glitches (i.e., transient noise artifacts) [55].

Seismic noise occurs because of the ground motion at the interferometer sites. This motion is $\sim 10^{-9}$ m/$\sqrt{\text{Hz}}$ at 10 Hz [56]. To provide isolation from this motion, the mirrors are suspended from quadruple pendulums [57]. The primary components of thermal noise are suspension thermal noise and coating Brownian noise. Suspension thermal noise occurs due to loss in the fused silica fibers used in the final suspension stage [31], whereas the coating Brownian noise (which is classified as a sensing noise) occurs due to the mechanical dissipation in the coatings [58]. Other types of sensing noise comprise many noise sources that are dominant at high frequencies, such as thermal fluctuations of the mirrors shape, optical losses, or photodetection inefficiency [59]. The noise budget of aLIGO can be found in Fig. 3.

Due to the classification above, we represent the sum of the seismic and the suspension thermal noise with $\hat{n}_F(\Omega)$, and the coating thermal noise with $\hat{n}_X(\Omega)$. We use the aLIGO noise budgets as given by the Python Gravitational Wave Interferometer Noise Calculator library (pygwinc) [60] and we model them with rational functions of Ω^2. The noise spectra are modeled by

$$S_F^{\mathrm{LIGO}}(\Omega) = \frac{\tau_F \alpha_{F_1}}{\left(\frac{\Omega}{\omega_F}\alpha_{F_2}\right)^{14} + 1}, \tag{19a}$$

$$S_X^{\mathrm{LIGO}}(\Omega) = \tau_{X_1}\left(\frac{\Omega}{\omega_X}\right)^2 \alpha_{X_1} + \tau_{X_2}\alpha_{X_2}, \tag{19b}$$

where $S_F^{\mathrm{LIGO}}(\Omega)$ is the spectrum of the force noise, and $S_X^{\mathrm{LIGO}}(\Omega)$ is the spectrum of the sensing noise. We model $S_F^{\mathrm{LIGO}}(\Omega)$ to decay as Ω^{-14} instead of Ω^{-16} (which is the expected behavior for quadruple suspension systems) since it performs better at approximating the global behavior. The power spectral densities are characterized by the time constants τ_F, τ_{X_1}, τ_{X_2} and cutoff frequencies ω_F, ω_X. The values of these parameters can be found in Appendix B, Table I. α_{F_1}, α_{F_2}, α_{X_1}, and α_{X_2} are dimensionless constants that will be used to change the noise curves in Sec. VI. Their effect on the noise curves can be seen in Fig. 4. If we set all of them to be unity, we get our model of aLIGO noise curves.

Even though the parameters of aLIGO are well known, they need to be recomputed since we are reducing the antisymmetric mode of the interferometer to a single cavity. The relation between the parameters of the antisymmetric mode and the parameters of the reduced cavity have already been computed [34], however we choose to work numerically and find the parameters of the reduced cavity G, γ, M, γ_m, ω_m, and L by fitting aLIGO's quantum noise spectrum found in pygwinc. The modeled classical and quantum noise curves can be found in Appendix C, Fig. 7. The fitted parameters can be found in Appendix B, Table II.

VI. ENTANGLEMENT IN aLIGO

In aLIGO, the spectrum is dominated by force noise for low frequencies and quantum noise for high frequencies, therefore we expect the sensing noise not to affect the entanglement significantly, which we observed with our numerics. Then, we focus on the effect of the force noise on the entanglement and use the parameters α_{F_1} and α_{F_2} to modify the force noise spectrum, and set $\alpha_{X_1} = \alpha_{X_2} = 1$ throughout all of the following subsections. We also introduce resonant modes to investigate the system as accurately as possible. Intuitively, we expect the entanglement to be destroyed in the presence of high classical noise levels.

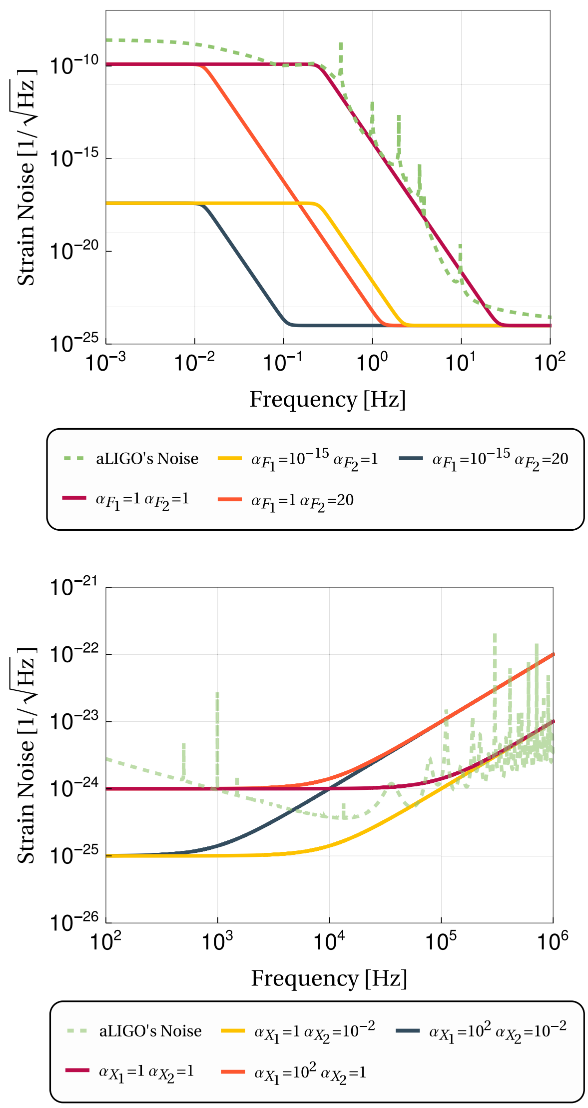

FIG. 4. Force (top row) and sensing noise (bottom row) spectra parametrized by α_{F_1}, α_{F_2}, α_{X_1}, and α_{X_2}. The effect of α_{F_1} is to rise and lower the nominal noise strength below the cutoff frequency and α_{F_2} shifts the cutoff frequency. Similarly, α_{X_1} shifts the cutoff frequency where the sensing noise starts increasing as Ω^2, whereas α_{X_2} shifts the nominal noise level.

A. Effect of force noise

First, we investigate the effect of the force noise spectrum on entanglement and we calculate the logarithmic negativity E_N as a function of α_{F_1} and α_{F_2} for both of the partitions described in Sec. III. For all pairs α_{F_1} and α_{F_2} here, we find larger logarithmic negativity values when we do not trace over the cavity. The results for the partition where we do not trace over the cavity can be found in Fig. 5. The amount of entanglement in the system diminishes when the force noise increases: that is, towards the bottom-right of the plot where α_{F_1} increases (proportional to the dc noise power) and α_{F_2} decreases (inversely proportional to the noise bandwidth), cf. Sec. V and Fig. 4. Our fit of aLIGO's force noise level is for $\alpha_{F_1} = \alpha_{F_2} = 1$, hence this plot is for a comparatively low level of force noise. Further to the bottom-right, the numerics

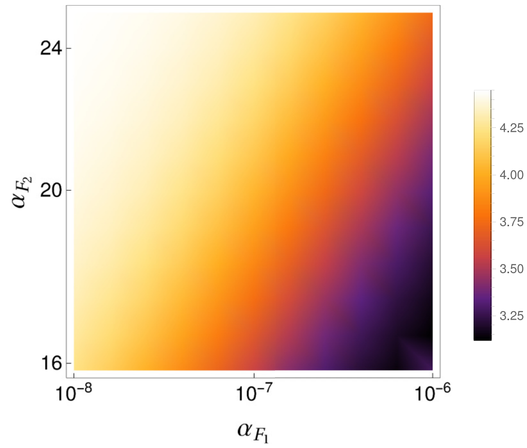

FIG. 5. The effect of the force noise spectrum on the logarithmic negativity when we do not trace over the cavity. Note that the force noise levels increase toward the bottom-right of the figure, and our fit of aLIGO's operation regime is for $\alpha_{F_1} = \alpha_{F_2} = 1$.

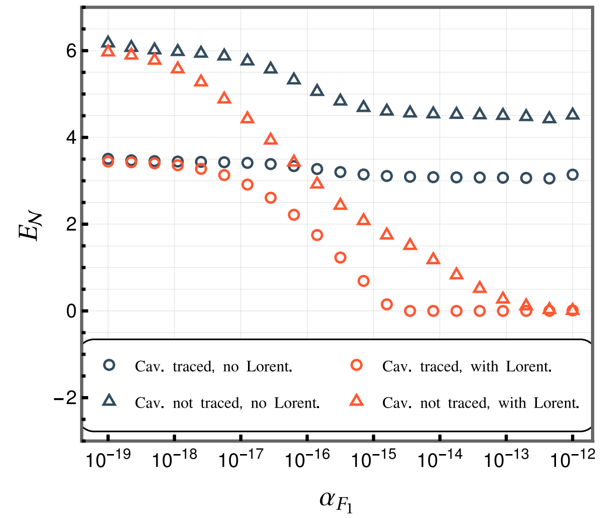

FIG. 6. The effect of resonant modes on the logarithmic negativity, $E_\mathcal{N}$, for both partitions. We see that the negativity reduces with increasing α_{F_1} or with the introduction of resonant modes. Note that $\alpha_{F_2} = 1$.

become unstable and do not converge due to the wide range of orders of magnitude entering the calculation; see Appendix E for a discussion of the numerical implementation. Therefore, we cannot give a definite answer about optomechanical entanglement in aLIGO with our model yet.

Next, we look for entanglement in the absence of the seismic noise, since it is the dominating contribution to the force noise of the system. Not being subjected to seismic noise is a realistic scenario for space-based gravitational-wave interferometers, such as the Laser Interferometer Space Antenna (LISA) [61]. For aLIGO, in the absence of seismic noise, suspension thermal noise dominates the spectrum for low frequencies, which is modeled as

$$S_{\mathrm{ST}}(\Omega) = \frac{\tau_{\mathrm{ST}}}{\left(\frac{\Omega}{\omega_{\mathrm{ST}}}\right)^8 + 1}, \tag{20}$$

similar to how the total force noise was modeled in Sec. V. The parameters τ_{ST} and ω_{ST} can be found in Table I. Without changing the other parameters in the system, we find that we can achieve negativities of 1.52 and 1.72 for the partitions where we do and do not trace over the cavity respectively. This means that, in the absence of seismic noise, aLIGO has stationary optomechanical entanglement in its current operating regime.

B. Effect of low-frequency resonances

Both the classical and the quantum noise curves contain many resonances, as can be seen from Fig. 3. The resonances in the seismic and suspension thermal noise arise from the displacement noises of the rigid-body resonant modes of the four-stage suspension system [57]. These modes can be modeled with a sum of Lorentzians multiplying the force noise spectrum defined in Eq. (19). Then, the new formula defining the spectrum of the force noise is given as

$$S_F^R(\Omega) = \frac{\tau_F \alpha_{F_1}}{\left(\frac{\Omega}{\omega_F}\alpha_{F_2}\right)^{14} + 1} \times \left(1 + \sum_i \frac{A_{v_i}^2}{(\Omega - \Omega_{v_i})^2 + \left(\frac{1}{2}\Gamma_{v_i}\right)^2}\right) \quad \text{with } \Omega > 0, \tag{21a}$$

$$S_F^R(\Omega) = S_F^R(-\Omega), \tag{21b}$$

where the sum is over the resonant modes. The parameters Ω_{v_i}, Γ_{v_i}, and A_{v_i} are the mode frequencies, full widths at half-maximum (FWHM), and the amplitudes of the Lorentzians, respectively, and they are listed in Appendix B, Table III for the modes with the biggest relative amplitudes.

We investigate the effect of the resonant modes on the entanglement. In Fig. 6, with low force noise guaranteeing well-behaved numerics and setting $\alpha_{F_2} = 1$, we plot $E_\mathcal{N}$ for noise curves with and without these modes (orange and gray, respectively) and for both partitions (circles when the cavity is traced out). We see explicitly here that there is more entanglement in the partition where we do not trace over the cavity. For low noise (low α_{F_1}), the negativity remains unchanged, hence the resonant modes do not affect the entanglement significantly in this regime. As the level of noise increases, resonant modes cause the logarithmic negativity to decrease faster than the negativities calculated without the resonant modes for both partitions. The system becomes separable when resonant modes are included for $\alpha_{F_1} \approx 10^{-15}$ and $\alpha_{F_1} \approx 10^{-12}$ when we do and do not trace over the cavity, respectively. It seems reasonable to expect that entanglement will not emerge when force noise becomes stronger. Hence, extrapolating $\alpha_{F_1} \to 1$, this is evidence (but not a rigorous proof) that aLIGO in its current operation regime (but without squeezed input) probably contains no optomechanical entanglement.

VII. DISCUSSION AND CONCLUSIONS

In this paper, we developed a framework to determine and quantify bipartite entanglement in an optomechanical system in the non-sideband-resolved regime in the presence of non-Markovian Gaussian noises. The main novelty of our work is to enable the study of non-Markovian noise drives, which are common in devices with low mechanical frequencies, typically associated with large/macroscopic masses. Hence, we focused on macroscopic entanglement and used a free mass with structural damping and coating Brownian noise as an initial example, and then aLIGO as a more detailed case study. However, non-Markovian noise can also be found in optomechanical systems with higher frequencies [29,30,62,63], and our framework can be applied to them in the same way. Besides improving the quality and accuracy of predictions, modeling non-Markovian dynamics is rich in interesting physics and possibly useful phenomena: for example, in Ref. [63], they find that squashing/squeezing the mechanical state is less demanding in the presence of structural damping compared to Markovian viscous damping.

We tested for bipartite entanglement by looking at the separability between the mechanical oscillator and (i) the outgoing light field, and (ii) the joint system of the cavity and the outgoing light field. For low levels of classical noise, we saw that the latter partition is more entangled compared to the former. However, for high levels of classical noise, we did not see a significant advantage in using one partition over the other.

In the low mechanical frequency regime, where the free-mass limit approximation holds, we found that the presence of entanglement is independent of the coherent optomechanical interaction strength and depends only on the relative strength of force and sensing noise. This result is similar to that already found in [4] for white noise drive. Beyond the free-mass limit approximation, by parametrizing the noise curves of aLIGO, we were able to find a region of noise curves where entanglement exists, and we showed that there is a tradeoff between the overall noise level and the cutoff frequency. Due to the high level of the current classical noise in aLIGO, we were not able to reach a definite conclusion in terms of the existence of entanglement in the system, even though it is unlikely to have a significant amount of entanglement based on our simulations. However, we saw that entanglement exists if we assume a system without seismic noise, even when the suspension thermal noise is still present. This is an important result since it shows that classical noises, even at very low frequencies, are able to demolish entanglement.

We also looked at how resonances in the noise curves of the system affect the amount of entanglement, and we saw that entanglement is more resistant (i.e., it disappears for higher levels of classical noise) for the partition where we test for the separability between the mechanical oscillator and the joint system of the cavity and the outgoing light field. For future work, we plan to develop better sampling strategies to overcome numerical instabilities.

ACKNOWLEDGMENTS

We thank the Chen Quantum Group for helpful discussions. S.D. and Y.C. acknowledge the support by the Simons Foundation (Award No. 568762). K.W., C.G., and M.A. received funding from the European Research Council (ERC) under the European Unions Horizon 2020 research and innovation program (Grant Agreement No. 951234), and from the Research Network Quantum Aspects of Spacetime (TURIS). K.H. was supported by the Deutsche Forschungsgemeinschaft (DFG, German Research Foundation) through Project-ID 274200144 SFB 1227 (projects A06) and Project-ID 390837967-EXC 2123.

APPENDIX A: TRANSFORMATION OF THE OPTOMECHANICAL HAMILTONIAN

Strictly speaking, the Hamiltonian in Eq. (1) is written in terms of Schrödinger operators. The symbol Ω in Eq. (1) is used to label a spatial mode which has a reduced wave number of Ω/c and a free oscillation frequency of Ω. More specifically, $\omega_0 + \Omega$ is used to indicate a spatial mode whose wave number is $(\omega_0 + \Omega)/c$, where c is the speed of light. We can also write the same Hamiltonian in the spatial domain. Following [35] and setting $c = 1$, we define

$$\hat{c}(z) = \int_{-\infty}^{\infty} \frac{d\Omega}{2\pi} \hat{c}(\omega_0 + \Omega) e^{i\Omega z}, \tag{A1}$$

which represents a spatial mode of the light field with wave number Ω—or a temporal mode of the free light field with frequency Ω, since we assume no dispersion. The Hamiltonian can then be rewritten as

$$\begin{aligned} H = {}& \hbar\omega_m \hat{B}^\dagger \hat{B} + \hbar\Delta \hat{A}^\dagger \hat{A} - \hbar G \hat{x}(\hat{A}^\dagger + \hat{A}) \\ & + i\hbar\sqrt{2\gamma}[\hat{A}^\dagger \hat{c}(z=0) - \hat{A}\hat{c}^\dagger(z=0)] \\ & - i\hbar \int_{-\infty}^{\infty} \hat{c}^\dagger(z) \partial_z \hat{c}(z)\, dz. \end{aligned} \tag{A2}$$

The only nonzero commutators for the creation and annihilation operators, as well as the spatial modes of the light field are

$$[\hat{c}(\omega_0 + \Omega), \quad \hat{c}^\dagger(\omega_0 + \Omega')] = 2\pi\delta(\Omega - \Omega'), \tag{A3a}$$

$$[\hat{c}(z), \quad \hat{c}^\dagger(z')] = \delta(z - z'), \tag{A3b}$$

where δ is the Dirac delta distribution.

APPENDIX B: PARAMETER TABLES

This Appendix contains the tables with the numerical values of the parameters used in modeling the classical and quantum noise curves, including the resonant modes. The parameters were calculated by minimizing the mean-squared error between the actual noise curves of aLIGO taken from pygwinc and the theoretical models, characterized by the parameters of interest, sampled logarithmically in frequency. Table I contains the parameters for the classical force and sensing noise in aLIGO defined in Eqs. (19), Table II contains the parameters of aLIGO introduced in the optomechanical Hamiltonian of Sec. II, and lastly, Table III contains the

TABLE I. Classical noise model parameters.

Parameter	Symbol	Value	Units
Force noise time constant	τ_F	1.6×10^{-20}	s
Force noise cutoff frequency	ω_F	$2\pi \times 0.25$	rad/s
Sensing noise time constant 1	τ_{X_1}	10^{-50}	s
Sensing noise time constant 2	τ_{X_2}	10^{-48}	s
Sensing noise cutoff frequency	ω_X	$2\pi \times 10^4$	rad/s
Suspension thermal noise time constant	τ_{ST}	3.1×10^{-35}	s
Suspension thermal noise cutoff frequency	ω_{ST}	$2\pi \times 1.9 \times 10^3$	rad/s

parameters of the resonant modes present in aLIGO's noise curves, modeled with Eq. (21).

APPENDIX C: NOISE MODEL

Our model for the total classical and quantum noise in aLIGO is displayed in Fig. 7. Note that the coating Brownian noise, which is the dominating classical noise source above ∼10 Hz, is modeled in a piecewise manner: a white noise in the 10–10^5 Hz band and a noise source increasing as Ω^2 for frequencies larger than 10^5 Hz. Even though the sensing noise in the 10–10^5 Hz band decreases as $\Omega^{0.8}$ in the power spectral density, we choose to model it with a frequency-independent white noise for simplified calculations. Our choice is justified since the quantum noise dominates over the coating Brownian noise in that region.

APPENDIX D: STRUCTURE OF THE COVARIANCE MATRIX

The mirror and the cavity, at $t = 0$, constitute two modes, whereas there are an infinite number of modes in the outgoing light field given by the quadratures $\hat{v}_1(t)$, $\hat{v}_2(t)$, $t \in (-\infty, 0)$. In continuum coordinates, we can first write down the commutator matrix,

$$\mathbf{K} = \begin{bmatrix} \mathbf{K}^B & & \\ & \mathbf{K}^A & \\ & & \mathbf{K}^v \end{bmatrix}, \tag{D1}$$

with

$$\mathbf{K}^A = \mathbf{K}^B = \begin{bmatrix} 0 & i \\ -i & 0 \end{bmatrix},$$

TABLE II. aLIGO parameters.

Parameter	Symbol	Value	Units
Mechanical resonant frequency	ω_m	$2\pi \times 0.9991$	rad/s
Mirror mass	M	9.446	kg
Cavity decay rate	γ	$2\pi \times 424.6$	rad/s
Arm length	L	3.995	km
Circulating power	P_c	322.7	kW
Laser wavelength	λ	1064	nm
Mechanical damping	γ_m	$2\pi \times 10^{-3}$	rad/s

TABLE III. Resonant mode parameters.

Parameter	Symbol	Value	Units
Mode frequency	Ω_{v_1}	$2\pi \times 0.441$	rad/s
	Ω_{v_2}	$2\pi \times 0.995$	rad/s
	Ω_{v_3}	$2\pi \times 1.98$	rad/s
	Ω_{v_4}	$2\pi \times 2.37$	rad/s
	Ω_{v_5}	$2\pi \times 3.38$	rad/s
	Ω_{v_6}	$2\pi \times 3.81$	rad/s
	Ω_{v_7}	$2\pi \times 9.73$	rad/s
Full width at half-maximum	Γv_1	$2\pi \times 1.92 \times 10^{-3}$	rad/s
	Γv_2	$2\pi \times 5.63 \times 10^{-5}$	rad/s
	Γv_3	$2\pi \times 2.11 \times 10^{-5}$	rad/s
	Γv_4	$2\pi \times 1.44 \times 10^{-1}$	rad/s
	Γv_5	$2\pi \times 1.45 \times 10^{-4}$	rad/s
	Γv_6	$2\pi \times 1.65 \times 10^{-3}$	rad/s
	Γv_7	$2\pi \times 1.03 \times 10^{-3}$	rad/s
Amplitude	A_{v_1}	159	rad/s
	A_{v_2}	93.8	rad/s
	A_{v_3}	538	rad/s
	A_{v_4}	235	rad/s
	A_{v_5}	353	rad/s
	A_{v_6}	27.4	rad/s
	A_{v_7}	78.0	rad/s

$$\mathbf{K}^v = \begin{bmatrix} 0 & i\delta(t-t') \\ -i\delta(t-t') & 0 \end{bmatrix}. \tag{D2}$$

Note that $\mathbf{K}^v$ is a 2×2 block matrix, but each block is infinite-dimensional, with columns and rows indexed by t and t', respectively. The indices t and t' each run through all negative real numbers, $(-\infty, 0]$. To represent these covariance matrices in a less ambiguous and more operational way, we shall adopt an index notation, in which j, k, l, m are discrete and run through 1 and 2, while t and t' are continuous and run through negative real numbers. We can then write

$$K^A_{jk} = i\epsilon_{jk},\; K^B_{lm} = i\epsilon_{lm},\; K^v_{lt,mt'} = i\epsilon_{lm}\delta(t-t'). \tag{D3}$$

Note that for $\mathbf{K}^v$ we have a two-dimensional row index (l, t), as well as a two-dimensional column index (m, t'), to label quadrature and arrival time.

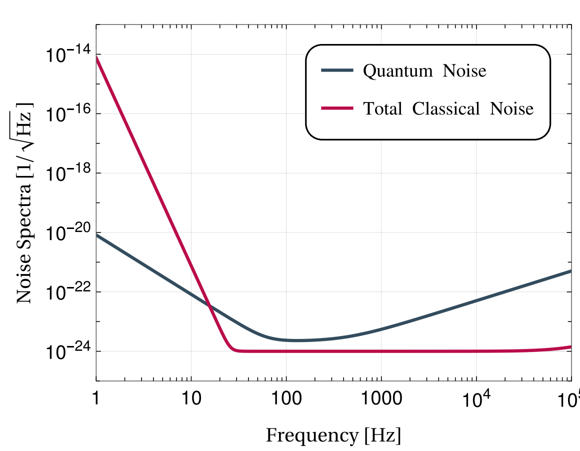

FIG. 7. Modeled noise spectrum for aLIGO.

The covariance matrix $\mathbf{V}$ of the system contains the steady-state correlations between the mechanical mode at $t = 0$, the cavity mode at $t = 0$, and the outgoing light field modes for $t < 0$. It can be written as

$$\mathbf{V} = \left[\begin{array}{cc|c} V^{BB} & V^{BA} & V^{Bv} \\ V^{AB} & V^{AA} & V^{Av} \\ \hline V^{vB} & V^{vA} & V^{vv} \end{array}\right] \equiv \begin{bmatrix} V^{QQ} & V^{Qv} \\ V^{vQ} & V^{vv} \end{bmatrix}. \tag{D4}$$

Here each of A and B represent two dimensions, while v represents an infinite number of dimensions. For computational purposes, we can group A and B together as Q, or

$$\hat{Q}_J = \hat{Q}_{(1,2,3,4)} = (\hat{B}_1, \hat{B}_2, \hat{A}_1, \hat{A}_2). \tag{D5}$$

Here we shall use upper-case Latin indices to run from 1 to 4 to label quadratures in the mechanical and cavity modes. We can write

$$V^{QQ}_{JK} = \frac{1}{2}\langle \hat{Q}_J\hat{Q}_K + \hat{Q}_K\hat{Q}_J\rangle = \int_0^\infty \frac{d\Omega}{2\pi} S_{Q_J Q_K}(\Omega), \tag{D6}$$

where the (one-sided) cross spectrum is defined via

$$S_{XY}(\Omega)\delta(\Omega - \Omega') = 2\pi \langle \hat{X}(\Omega)\hat{Y}^\dagger(\Omega') + \hat{Y}^\dagger(\Omega')\hat{X}(\Omega)\rangle, \tag{D7}$$

and they can be obtained from solutions to the Heisenberg equations, as well as the spectra

$$S_{u_i u_j}(\Omega) = \delta_{ij}, \tag{D8}$$

and the prescriptions we use for the spectra of $S_{n_X}(\Omega)$ and $S_{n_F}(\Omega)$. The uncorrelated white spectra between $\hat{u}_1$ and $\hat{u}_2$ in Eq. (D8) result from the ingoing light field being in its vacuum state. We shall discuss the magnitude and frequency dependence of $S_{n_X}(\Omega)$ and $S_{n_F}(\Omega)$ in depth in the next Appendix.

For elements that involve v, we shall still use lt for column indices and mt' for row indices. We then have

$$\begin{aligned} V^{Qv}_{J,mt'} &= \frac{1}{2}\langle \hat{Q}_J\hat{v}_m(t') + \hat{v}_m(t')\hat{Q}_J\rangle \\ &= \frac{1}{2}\int_{-\infty}^{+\infty} \frac{d\Omega}{2\pi} S_{Q_J v_m}(\Omega) e^{i\Omega t'} \end{aligned} \tag{D9}$$

and

$$\begin{aligned} V^{vv}_{lt,mt'} &= \frac{1}{2}\langle \hat{v}_l(t)\hat{v}_m(t') + \hat{v}_m(t)\hat{v}_l(t')\rangle \\ &= \frac{1}{2}\int_{-\infty}^{+\infty} \frac{d\Omega}{2\pi} S_{v_l v_m}(\Omega) e^{-i\Omega(t-t')}. \end{aligned} \tag{D10}$$

Note that $V^{Qv}_{J,mt'} = V^{vQ}_{mt',J}$.

In numerical computations, we will have to convert the continuum of $t, t' \leqslant 0$ into a finite grid. This means we will sample a finite duration T with a step size of Δt. We shall still use lower-case Latin indices to run from 1 to 2, and upper-case Latin indices to run from 1 to 4, while we use Greek indices, for example, $\alpha = 0, 1, 2, \ldots, T/\Delta t \equiv \mathcal{N} - 1$, to replace t. We shall write

$$K^v_{lt,mt'} \to K^v_{l\alpha,m\alpha'} = i\epsilon_{lm}\delta_{\alpha\alpha'}. \tag{D11}$$

Note that a Kronecker δ now replaces the Dirac δ. For the covariance matrix, we replace

$$V^{Qv}_{J,mt'} \to V^{Qv}_{J,m\alpha'} = \frac{\sqrt{\Delta t}}{2}\langle \hat{Q}_J\hat{v}_m(t_{\alpha'}) + \hat{v}_m(t_{\alpha'})\hat{Q}_J\rangle, \tag{D12}$$

which are $(4 \times 2\mathcal{N})$- and $(2\mathcal{N} \times 4)$-dimensional matrices (with $V^{vQ}_{J,mt'}$), and

$$V^{vv}_{lt,mt'} \to V^{vv}_{l\alpha,m\alpha'} = \frac{\Delta t}{2}\langle \hat{v}_l(t_\alpha)\hat{v}_m(t_{\alpha'}) + \hat{v}_m(t_\alpha)\hat{v}_l(t_{\alpha'})\rangle, \tag{D13}$$

which is a $(2\mathcal{N} \times 2\mathcal{N})$-dimensional matrix. For the discrete sampling times, we have defined

$$t_\alpha = -\left(\alpha + \tfrac{1}{2}\right)\Delta t, \tag{D14}$$

where the additional $\frac{1}{2}\Delta t$ provides a faster convergence in numerics. The entire covariance matrix is then $[(2\mathcal{N} + 4) \times (2\mathcal{N} + 4)]$-dimensional.

Our particular convention of inserting Δt at various places of the matrix is associated with our convention of discretizing vectors. For a generic variable, in the continuum form, we can always express it as

$$\begin{aligned} X &= \alpha^j\hat{A}_j + \beta^j\hat{B}_j + \int_{-\infty}^0 \xi^j(t)\hat{v}_j(t)dt \\ &= \gamma^J\hat{Q}_J + \int_{-\infty}^0 \xi^j(t)\hat{v}_j(t)dt, \end{aligned} \tag{D15}$$

where we have used upper indices for vector components, and we have grouped α^j and β^j into γ^J. The variance of X, which is formally written as $\mathbf{X}^\dagger\mathbf{V}\mathbf{X}$, will then be

$$\begin{aligned} \mathbf{X}^\dagger\mathbf{V}\mathbf{X} =& \frac{1}{2}\gamma^J\langle \hat{Q}_J\hat{Q}_K + \hat{Q}_K\hat{Q}_J\rangle\gamma^K \\ &+ \int_{-\infty}^0 \gamma^J\langle \hat{Q}_J\hat{v}_m(t') + \hat{v}_m(t')\hat{Q}_J\rangle\xi^m(t')dt' \\ &+ \frac{1}{2}\iint_{-\infty}^0 \xi^l(t)\langle \hat{v}_l(t)\hat{v}_m(t') + \hat{v}_m(t)\hat{v}_l(t')\rangle\xi^m(t')dtdt'. \end{aligned} \tag{D16}$$

As we convert the integrals in Eq. (D16) into summations, $\int$ will become Σ, while dt will become Δt. We shall take

$$\xi^{m\alpha} = \xi^m(t_\alpha)\sqrt{\Delta t}. \tag{D17}$$

Together with Eqs. (D12) and (D13), the fully discretized version of Eq. (D16) will then be

$$\begin{aligned} \mathbf{X}^\dagger\mathbf{V}\mathbf{X} =& \gamma^J V^{QQ}_{JK}\gamma^K + \gamma^J V^{Qv}_{J,m\alpha}\xi^{m\alpha} + \xi^{l\beta}V^{vQ}_{l\beta,K}\gamma^K \\ &+ \xi^{l\alpha}V^{vv}_{l\alpha,m\beta}\xi^{m\beta}. \end{aligned} \tag{D18}$$

In this convention, the usual vector norm for the discretized version of a function of time coincides with the L^2-norm of that function. It can also be checked that discretized matrices in Eqs. (D11)–(D13), when contracted with vectors in this convention, lead to the appropriate integrals. Note that if a $\delta(t_\alpha - t'_\alpha)$ shows up in Eq. (D13), we will take $\Delta t\delta(t_\alpha - t'_\alpha) \to \delta_{\alpha\alpha'}$, as in Eq. (D11).

Corresponding to the discussion at the end of Sec. III (also shown in Fig. 1), here we consider entanglement between (i) mass at $t = 0$ and the outgoing light field that had emerged during $t \leqslant 0$, and (ii) mass and the joint system of the cavity mode as well as light that had emerged during $t \leqslant 0$. In case (i), we simply throw away elements involving A in both $\mathbf{K}$ and $\mathbf{V}$, while in case (ii) we consider the full matrices. In both cases, $\mathbf{V}_{\rm pt}$ is obtained by adding a minus sign to the column involving $\hat{B}_2$ and the row involving $\hat{B}_2$—but not the diagonal element at which they intersect.

APPENDIX E: NUMERICAL IMPLEMENTATION FOR ALIGO's NOISE

In our simulations, we use $dt = 0.25$ ms and $T = 0.1$ s, which corresponds to sampling the light field at 4000 Hz and working with the outgoing field emitted from the cavity between $t = -0.1$ and 0 s. We achieve numerical convergence with these parameters. To quantify the amount of entanglement in the system, we use the logarithmic negativity defined in Eq. (14). However, this is possible only for low levels of classical noise. For high levels of classical noise, classical correlations dominate over quantum correlations, which causes the cross-correlation values in the system to cover a wide range of orders of magnitude, mostly due to the 14th power of Ω in our force noise model Eq. (19). For aLIGO parameters, the entries of the covariance matrix span about 20 orders of magnitudes, while we attempt to find a symplectic eigenvalue of order 1—this is numerically an extremely challenging problem.

Numerical errors also arise because of time-binning with an insufficient resolution. Thus, we lose precision on the numerically determined covariance matrices. This affects the smallest symplectic eigenvalue $\tilde{\nu}_{\rm min}$ to the point that it cannot be used to measure entanglement with the logarithmic negativity. Numerical imprecision can lead to covariance matrices that do not satisfy Heisenberg uncertainty bound Eq. (12), they thus do not correspond to a *bona fide* state and we call them *nonphysical*. One way to get around this loss of precision is to use the PPT criterion as a yes/no test only, renouncing the magnitude information of $\tilde{\nu}_{\rm min}$. The sampling frequency during time binning should be higher than the Nyquist rate of the system (i.e., twice the largest frequency in the system), since the entries of the covariance matrix contain correlations from all frequencies. In our system, the largest frequency is the cavity decay rate $\gamma = 424$ Hz. Therefore, we choose $dt < 1/(2 \times 424) \approx 1.2$ ms. However, as we decrease dt, we are limited by computational resources, such as the RAM size, or time. The parameter dt is limited to an optimal range determined by this tradeoff. We thus develop the following strategy: we first quantify the amount of numerical errors in the system by computing the most negative eigenvalue (if it exists) of $\mathbf{V} + \frac{1}{2}\mathbf{K}$ before and after the partial transpose operation, denoted as $\lambda_{\mathcal{B}}$ and $\lambda_{\mathcal{N}}$, respectively. Then, we decide that entanglement exists if $\lambda_{\mathcal{B}} > 0$ and $\lambda_{\mathcal{N}} < 0$, or if $\lambda_{\mathcal{B}} < 0$ and $|\lambda_{\mathcal{N}}| \gg |\lambda_{\mathcal{B}}|$. Furthermore, we decide that the system is separable if $\lambda_{\mathcal{B}} > 0$ and $\lambda_{\mathcal{N}} > 0$.

Two case studies about this strategy can be found in Fig. 8, where we fix $T = 0.1$ s, change dt, and examine how $\lambda_{\mathcal{N}}$ and $\lambda_{\mathcal{B}}$ change by plotting $\lambda_{\mathcal{N}}$ and $\lambda_{\mathcal{B}}$. We decide on entanglement if $\lambda_{\mathcal{B}} \geqslant 0$ and $\lambda_{\mathcal{N}} < 0$, or $\lambda_{\mathcal{B}} < 0$, $\lambda_{\mathcal{N}} < 0$, and $|\lambda_{\mathcal{N}}| \geqslant 100|\lambda_{\mathcal{B}}|$. Our criteria for convergence is a relative change smaller than 5% for both $\lambda_{\mathcal{N}}$ and $\lambda_{\mathcal{B}}$ as we change dt. In Fig. 8(a), we work with a low level of classical force noise and set $\alpha_{F_1} = 10^{-15}$, $\alpha_{F_2} = 15$ in Eq. (19). We see that $\lambda_{\mathcal{N}}$ and $\lambda_{\mathcal{B}}$ converge with $\lambda_{\mathcal{N}}$ changing by 0.053%, 0.068%, and $\lambda_{\mathcal{B}}$ changing by 4.9%, 0.77% before and after tracing over the cavity, respectively, for $dt = 0.1$ ms. The system is entangled for both partitions since $\lambda_{\mathcal{B}} \geqslant 0$ and $\lambda_{\mathcal{N}} < 0$. Furthermore, $\lambda_{\mathcal{B}}$ becomes positive and converges after $dt \sim 1$ ms, or a sampling frequency of 1000 Hz, consistent with the discussion above relating physicality to Nyquist rate of ~850 Hz. We also see that $\lambda_{\mathcal{N}}$ converges for similar values of dt from Fig. 8(a).

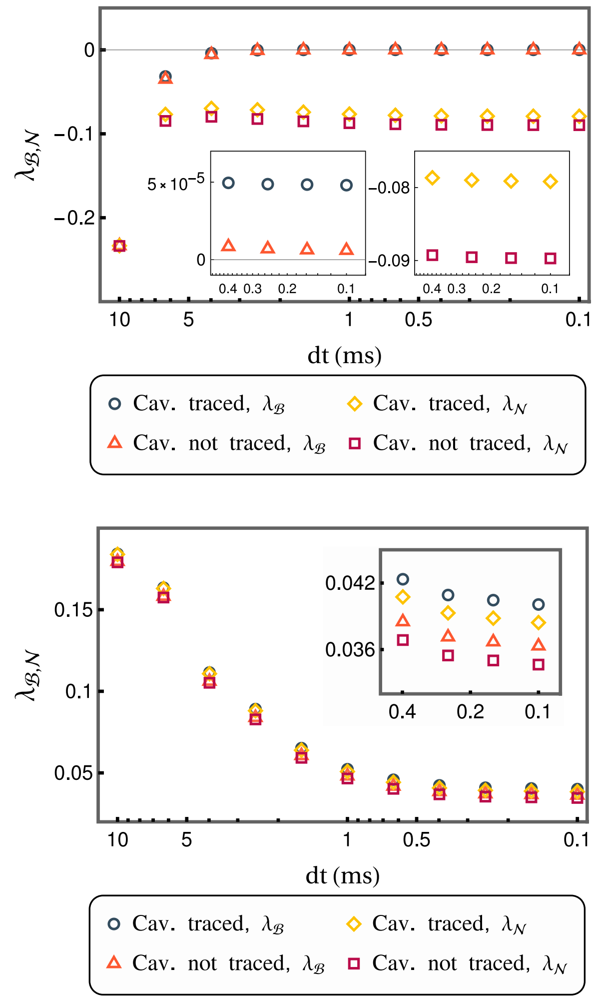

FIG. 8. $\lambda_{\mathcal{B}}$ and $\lambda_{\mathcal{N}}$ for $\alpha_{F_1} = 10^{-15}$ and $\alpha_{F_2} = 15$ [top row, (a)]; $\alpha_{F_1} = 10^{-8}$, $\alpha_{F_2} = 10$, and $\alpha_{X_2} = 10^3$ [bottom row, (b)]. We set $T = 0.1$ s and $dt \in [0.1, 10]$ ms. Note that dt decreases to the right of the plots. In (a), entanglement exists for both partitions, and $\lambda_{\mathcal{B}}(\lambda_{\mathcal{N}})$ is replotted in the inset on the left (right) for $dt \in [0.1, 0.5]$ ms. In (b), the state is separable for both partitions, and $\lambda_{\mathcal{B}}$ and $\lambda_{\mathcal{N}}$ are replotted in the inset for $dt \in [0.1, 0.5]$ ms.

In Fig. 9, we plot the light-field section of the eigenvector associated with the (converged) minimal eigenvalue of $\mathbf{V}_{\rm pt} + \frac{1}{2}\mathbf{K}$, for the partition where we do not trace over the cavity and with $\alpha_{F_1} = 10^{-15}$, $\alpha_{F_2} = 15$. It corresponds to a temporal mode of the free electromagnetic field outside the cavity. It is that particular mode associated with the (sole) negative eigenvalue that is entangled with the joint system mechanics plus cavity. The four curves correspond to the real and imaginary parts of $\hat{v}_1(t)$ and $\hat{v}_2(t)$. They have the form of smooth decaying oscillations with the same frequency and decay rate, but differing by a phase. This form of the

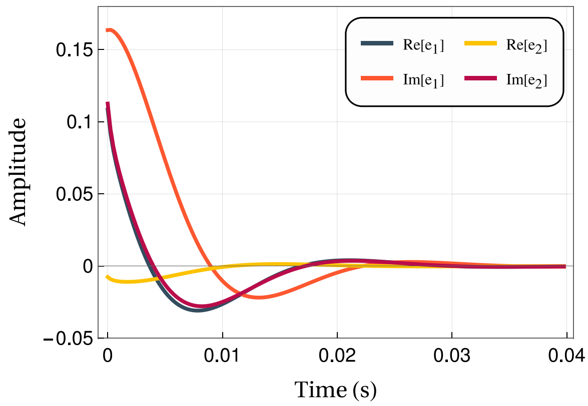

FIG. 9. The real and imaginary parts of the eigenvector for the negative eigenvalue of $\mathbf{V}_{\rm pt} + \frac{1}{2}\mathbf{K}$ for $\alpha_{F_1} = 10^{-15}$, $\alpha_{F_2} = 15$, denoted by e_1 and e_2, which correspond to the first and second halves of the entire eigenvector, respectively. The reason behind this slicing is the block-matrix structure of the light-field sector of the covariance matrix. Furthermore, since the light field modes are continuous in time, e_1 and e_2 are also functions of time.

mode functions was predicted for a white force noise in [6], which gives us confidence in the correctness of our study. Also, exponentially decaying demodulation pulses were used to demonstrate optomechanical entanglement [8,16] and proposed for a demonstration in the stationary regime [23]. We fit functions in the form of $e^{-\gamma_* t}\sin(\omega_* t + \theta)$ to each curve, which results in $\omega_*/(2\pi) \approx 40$ Hz, and $\gamma_*/(2\pi) \approx 25$ Hz.

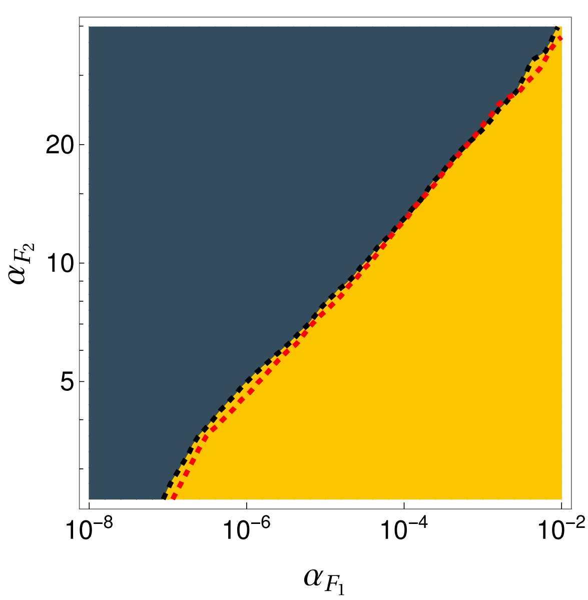

FIG. 10. Contour plot depicting the effect of the force noise spectrum on our numerical precision for both partitions. The force noise levels increase toward the bottom-right of the figure. The black and the red dashed lines separate the regions where numerics converge from the regions where numerics fail for the partition where we do and do not trace over the cavity, respectively. The region where numerics converge for both partitions is marked in gray, whereas numerics fail for both partitions toward the bottom right of the figure, past the red dashed line, in the yellow region.

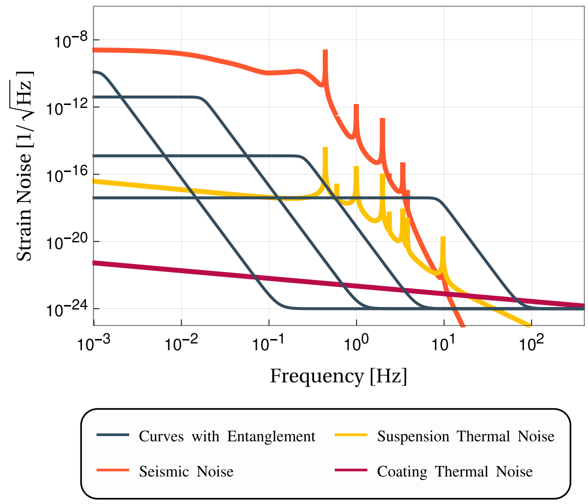

FIG. 11. Examples of force noise spectra along the boundary where we lose numerical precision (defined with $|\lambda_{\mathcal{N}}| = 100|\lambda_{\mathcal{B}}|$) for the partition where we do not trace over the cavity, plotted in black. aLIGO noise curves are also plotted for comparison. The black curves are parametrized with (from left to right) $\alpha_{F_1} = 1$ and $\alpha_{F_2} = 200$; $\alpha_{F_1} = 10^{-3}$ and $\alpha_{F_2} = 14$; $\alpha_{F_1} = 10^{-10}$ and $\alpha_{F_2} = 1$; and $\alpha_{F_1} = 10^{-15}$ and $\alpha_{F_2} = 0.029$.

In the frequency domain, exponentially decaying harmonic oscillations are Lorentzians, centered at $\pm\omega_*$ and with a bandwidth (FWHM) $2\gamma_*$. In aLIGO's noise budget (Fig. 3), these Lorentzians are on the low-frequency side of the low-noise band and their halfwidth at half-maximum to the left crosses the quantum noise, where it is not yet dominated by suspension thermal and seismic noises—although we saw in Sec. VI A that the latter is probably the main mechanism preventing optomechanical entanglement. We add that Lorentzians are heavy-tail distributions, being a possible reason why even lower frequency components matter.

In Fig. 8(b), we set $\alpha_{F_1} = 10^{-8}$, $\alpha_{F_2} = 10$, and $\alpha_{X_2} = 10^3$, causing the sensing noise to dominate over quantum noise for frequencies in the 30–2000 Hz band. We again see that $\lambda_{\mathcal{N}}$ and $\lambda_{\mathcal{B}}$ converge with $\lambda_{\mathcal{N}}$ changing by 1.3%, 1.2%, and $\lambda_{\mathcal{B}}$ changing by 1.2%, 1.1% before and after tracing over the cavity, respectively, for $dt = 0.1$ ms. Since $\lambda_{\mathcal{B}}$ and $\lambda_{\mathcal{N}}$ are positive for both partitions, we conclude that there is no entanglement in the system for either partition. When we increase the classical noise level, we see that convergence is much harder to achieve. Furthermore, $\lambda_{\mathcal{B}}$ and $\lambda_{\mathcal{N}}$ are negative, and $\lambda_{\mathcal{B}} \sim \lambda_{\mathcal{N}}$ for every value of dt regardless of when we do or do not trace over the cavity. Therefore, we cannot conclude that there is entanglement for either of the partitions. These case studies show that we can use $\lambda_{\mathcal{B}}$ as an indicator of the "nonphysicality" of the covariance matrix $\mathbf{V}$ introduced by finite-sampling and high levels of classical noise in the system, and that the negativity of $\lambda_{\mathcal{N}}$ is not enough to decide on entanglement when we consider the numerics.

For our model of aLIGO's non-Markovian noises, Eqs. (19), we study the numerical stability of broad noise regimes, parametrized by the pair α_{F_j}, $j = 1, 2$. We set $\alpha_{X_j} = 1$, $j = 1, 2$, since we saw that force noise had a greater impact on numerical stability than sensing noise in our simulations for aLIGO's noise. In Fig. 10, we plot the boundary between noise regimes where the numerics converge and the computed covariance matrices are physical (in gray) and those regimes where the numerics fail (either at converging or at generating physical covariance matrices or both) with the available computing resources (in yellow). As a matter of fact, in all the operation regimes in the gray region where the numerics work, the system is entangled. This means that our model predicts optomechanical entanglement in aLIGO if its classical noise is in this gray region. Recall that the current status of aLIGO corresponds to $\alpha_{F_j} = \alpha_{X_j} = 1$, $j = 1, 2$, far to the bottom-right in the undecidable yellow region.

If we follow the red dashed line in Fig. 10, we continuously sample the force noise spectrum over the boundary where our numerics converge, and the system is entangled, for the partition where we do not trace over the cavity. This boundary corresponds to a lower limit of the maximum amount of classical noise allowed in the system in order to have entanglement. We plot some of these noise curves in Fig. 11. Note that if we set α_{F_1} or α_{F_2} to be unity, the corresponding pairs of α_{F_1}, α_{F_2} situated on this boundary would be $\alpha_{F_1} = 1$ and $\alpha_{F_2} \geqslant 200$, or for $\alpha_{F_2} = 1$ and $\alpha_{F_1} \leqslant 10^{-10}$. The corresponding noise curves are also plotted in Fig. 11.

---

[1] C. Genes, A. Mari, D. Vitali, and P. Tombesi, Quantum effects in optomechanical systems, in *Advances in Atomic Molecular and Optical Physics* (Academic, San Diego, California, 2009), Vol. 57, Chap. 2, pp. 33–86.

[2] S. G. Hofer and K. Hammerer, Entanglement-enhanced time-continuous quantum control in optomechanics, Phys. Rev. A **91**, 033822 (2015).

[3] C. Genes, A. Mari, P. Tombesi, and D. Vitali, Robust entanglement of a micromechanical resonator with output optical fields, Phys. Rev. A **78**, 032316 (2008).

[4] H. Miao, S. Danilishin, H. Müller-Ebhardt, and Y. Chen, Achieving ground state and enhancing optomechanical entanglement by recovering information, New J. Phys. **12**, 083032 (2010).

[5] H. Miao, S. Danilishin, H. Müller-Ebhardt, H. Rehbein, K. Somiya, and Y. Chen, Probing macroscopic quantum states with a sub-heisenberg accuracy, Phys. Rev. A **81**, 012114 (2010).

[6] H. Miao, S. Danilishin, and Y. Chen, Universal quantum entanglement between an oscillator and continuous fields, Phys. Rev. A **81**, 052307 (2010).

[7] S. L. Danilishin, F. Y. Khalili, and H. Miao, Advanced quantum techniques for future gravitational-wave detectors, Liv. Rev. Relativ. **22**, 2 (2019).

[8] S. G. Hofer, W. Wieczorek, M. Aspelmeyer, and K. Hammerer, Quantum entanglement and teleportation in pulsed cavity optomechanics, Phys. Rev. A **84**, 052327 (2011).

[9] M. Aspelmeyer, T. J. Kippenberg, and F. Marquardt, Cavity optomechanics, Rev. Mod. Phys. **86**, 1391 (2014).

[10] S. Barzanjeh, E. S. Redchenko, M. Peruzzo, M. Wulf, D. P. Lewis, G. Arnold, and J. M. Fink, Stationary entangled radiation from micromechanical motion, Nature (London) **570**, 480 (2019).

[11] J. Chen, M. Rossi, D. Mason, and A. Schliesser, Entanglement of propagating optical modes via a mechanical interface, Nat. Commun. **11**, 943 (2020).

[12] R. Riedinger, A. Wallucks, I. Marinković, C. Löschnauer, M. Aspelmeyer, S. Hong, and S. Gröblacher, Remote quantum entanglement between two micromechanical oscillators, Nature (London) **556**, 473 (2018).

[13] C. F. Ockeloen-Korppi, E. Damskägg, J.-M. Pirkkalainen, M. Asjad, A. A. Clerk, F. Massel, M. J. Woolley, and M. A. Sillanpää, Stabilized entanglement of massive mechanical oscillators, Nature (London) **556**, 478 (2018).

[14] S. Kotler, G. A. Peterson, E. Shojaee, F. Lecocq, K. Cicak, A. Kwiatkowski, S. Geller, S. Glancy, E. Knill, R. W. Simmonds, J. Aumentado, and J. D. Teufel, Direct observation of deterministic macroscopic entanglement, Science **372**, 622 (2021).

[15] R. A. Thomas, M. Parniak, C. Østfeldt, C. B. Møller, C. Bærentsen, Y. Tsaturyan, A. Schliesser, J. Appel, E. Zeuthen, and E. S. Polzik, Entanglement between distant macroscopic mechanical and spin systems, Nat. Phys. **17**, 228 (2021).

[16] T. A. Palomaki, J. D. Teufel, R. W. Simmonds, and K. W. Lehnert, Entangling mechanical motion with microwave fields, Science **342**, 710 (2013).

[17] O. Romero-Isart, Quantum superposition of massive objects and collapse models, Phys. Rev. A **84**, 052121 (2011).

[18] H. Müller-Ebhardt, H. Rehbein, R. Schnabel, K. Danzmann, and Y. Chen, Entanglement of macroscopic test masses and the standard quantum limit in laser interferometry, Phys. Rev. Lett. **100**, 013601 (2008).

[19] R. Schnabel, Einstein-Podolsky-Rosen–Entangled motion of two massive objects, Phys. Rev. A **92**, 012126 (2015).

[20] M. Wang, X.-Y. Lü, Y.-D. Wang, J. Q. You, and Y. Wu, Macroscopic quantum entanglement in modulated optomechanics, Phys. Rev. A **94**, 053807 (2016).

[21] S. Pirandola, D. Vitali, P. Tombesi, and S. Lloyd, Macroscopic entanglement by entanglement swapping, Phys. Rev. Lett. **97**, 150403 (2006).

[22] M. Ludwig, K. Hammerer, and F. Marquardt, Entanglement of mechanical oscillators coupled to a nonequilibrium environment, Phys. Rev. A **82**, 012333 (2010).

[23] C. Gut, K. Winkler, J. Hoelscher-Obermaier, S. G. Hofer, R. M. Nia, N. Walk, A. Steffens, J. Eisert, W. Wieczorek, J. A. Slater, M. Aspelmeyer, and K. Hammerer, Stationary optomechanical entanglement between a mechanical oscillator and its measurement apparatus, Phys. Rev. Res. **2**, 033244 (2020).

[24] D. Vitali, S. Gigan, A. Ferreira, H. R. Böhm, P. Tombesi, A. Guerreiro, V. Vedral, A. Zeilinger, and M. Aspelmeyer, Optomechanical entanglement between a movable mirror and a cavity field, Phys. Rev. Lett. **98**, 030405 (2007).

[25] M. Paternostro, D. Vitali, S. Gigan, M. S. Kim, C. Brukner, J. Eisert, and M. Aspelmeyer, Creating and probing multipartite macroscopic entanglement with light, Phys. Rev. Lett. **99**, 250401 (2007).

[26] V. Giovannetti and D. Vitali, Phase-noise measurement in a cavity with a movable mirror undergoing quantum brownian motion, Phys. Rev. A **63**, 023812 (2001).

[27] P. R. Saulson, Thermal noise in mechanical experiments, Phys. Rev. D **42**, 2437 (1990).

[28] A. R. Neben, T. P. Bodiya, C. Wipf, E. Oelker, T. Corbitt, and N. Mavalvala, Structural thermal noise in gram-scale mirror oscillators, New J. Phys. **14**, 115008 (2012).
[29] S. Fedorov, V. Sudhir, R. Schilling, H. Schütz, D. Wilson, and T. Kippenberg, Evidence for structural damping in a high-stress silicon nitride nanobeam and its implications for quantum optomechanics, Phys. Lett. A **382**, 2251 (2018).
[30] S. Gröblacher, A. Trubarov, N. Prigge, G. D. Cole, M. Aspelmeyer, and J. Eisert, Observation of non-Markovian micromechanical brownian motion, Nat. Commun. **6**, 7606 (2015).
[31] J. Aasi *et al.*, Advanced ligo, Class. Quantum Grav. **32**, 074001 (2015).
[32] H. Yu and members of the LIGO Scientific Collaboration, Quantum correlations between light and the kilogram-mass mirrors of ligo, Nature (London) **583**, 43 (2020).
[33] The quantum noise's beating of the SQL is only inferred by subtracting a classical noise floor that was obtained through calibration.
[34] A. Buonanno and Y. Chen, Scaling law in signal recycled laser-interferometer gravitational-wave detectors, Phys. Rev. D **67**, 062002 (2003).
[35] Y. Chen, Macroscopic quantum mechanics: Theory and experimental concepts of optomechanics, J. Phys. B **46**, 104001 (2013).
[36] We use the convention $\mathcal{F}\{f(t)\} = \int_{-\infty}^{\infty} f(t)e^{i\omega t}dt$.
[37] C. M. Caves and B. L. Schumaker, New formalism for two-photon quantum optics. I. quadrature phases and squeezed states, Phys. Rev. A **31**, 3068 (1985).
[38] B. L. Schumaker and C. M. Caves, New formalism for two-photon quantum optics. II. mathematical foundation and compact notation, Phys. Rev. A **31**, 3093 (1985).
[39] S. L. Danilishin and F. Y. Khalili, Quantum measurement theory in gravitational-wave detectors, Liv. Rev. Relativ. **15**, 5 (2012).
[40] R. Kubo, The fluctuation-dissipation theorem, Rep. Prog. Phys. **29**, 255 (1966).
[41] H. J. Kimble, Y. Levin, A. B. Matsko, K. S. Thorne, and S. P. Vyatchanin, Conversion of conventional gravitational-wave interferometers into quantum nondemolition interferometers by modifying their input and/or output optics, Phys. Rev. D **65**, 022002 (2001).
[42] A. Peres, Separability criterion for density matrices, Phys. Rev. Lett. **77**, 1413 (1996).
[43] G. Adesso and F. Illuminati, Entanglement in continuous-variable systems: recent advances and current perspectives, J. Phys. A **40**, 7821 (2007).
[44] R. F. Werner and M. M. Wolf, Bound entangled gaussian states, Phys. Rev. Lett. **86**, 3658 (2001).
[45] R. Simon, Peres-Horodecki separability criterion for continuous variable systems, Phys. Rev. Lett. **84**, 2726 (2000).
[46] G. Vidal and R. F. Werner, Computable measure of entanglement, Phys. Rev. A **65**, 032314 (2002).
[47] A. Serafini, *Quantum Continuous Variables* (CRC, Boca Raton, FL, 2017).
[48] K. Somiya *et al.*, Detector configuration of Kagra the Japanese cryogenic gravitational-wave detector, Class. Quantum Grav. **29**, 124007 (2012).
[49] F. Acernese *et al.*, Advanced virgo: A second-generation interferometric gravitational wave detector, Class. Quantum Grav. **32**, 024001 (2015).
[50] J. Cripe, N. Aggarwal, R. Lanza, A. Libson, R. Singh, P. Heu, D. Follman, G. D. Cole, N. Mavalvala, and T. Corbitt, Measurement of quantum back action in the audio band at room temperature, Nature (London) **568**, 364 (2019).
[51] K. Komori, Y. Enomoto, C. P. Ooi, Y. Miyazaki, N. Matsumoto, V. Sudhir, Y. Michimura, and M. Ando, Attonewton-meter torque sensing with a macroscopic optomechanical torsion pendulum, Phys. Rev. A **101**, 011802(R) (2020).
[52] V. B. Braginsky, F. Y. Khalili, and K. S. Thorne, *Quantum Measurement* (Cambridge University Press, Cambridge, 1992).
[53] G. I. González and P. R. Saulson, Brownian motion of a torsion pendulum with internal friction, Phys. Lett. A **201**, 12 (1995).
[54] To find spectra of the form of Eqs. (16), one assumes the free-mass and high-Q limits where the mechanical susceptibility behaves as $1/\Omega^2$; additionally, one must be in frequency ranges where S_{n_F} and S_{n_X} are constant polynomial rolloff—typical at frequencies above the resonance of suspended oscillators.
[55] B. P. Abbott *et al.*, A guide to LIGO–virgo detector noise and extraction of transient gravitational-wave signals, Class. Quantum Grav. **37**, 055002 (2020).
[56] D. V. Martynov *et al.*, Sensitivity of the advanced ligo detectors at the beginning of gravitational wave astronomy, Phys. Rev. D **93**, 112004 (2016).
[57] S. M. Aston *et al.*, Update on quadruple suspension design for advanced ligo, Class. Quantum Grav. **29**, 235004 (2012).
[58] Y. T. Liu and K. S. Thorne, Thermoelastic noise and homogeneous thermal noise in finite sized gravitational-wave test masses, Phys. Rev. D **62**, 122002 (2000).
[59] H. Müller-Ebhardt, H. Rehbein, C. Li, Y. Mino, K. Somiya, R. Schnabel, K. Danzmann, and Y. Chen, Quantum-state preparation and macroscopic entanglement in gravitational-wave detectors, Phys. Rev. A **80**, 043802 (2009).
[60] J. G. Rollins, E. Hall, C. Wipf, and L. McCuller, pygwinc: Gravitational Wave Interferometer Noise Calculator, Astrophysics Source Code Library, record ascl:2007.020 (2020), ascl:2007.020.
[61] G. Wanner, Space-based gravitational wave detection and how lisa pathfinder successfully paved the way, Nat. Phys. **15**, 200 (2019).
[62] S. Gröblacher, J. B. Hertzberg, M. R. Vanner, G. D. Cole, S. Gigan, K. C. Schwab, and M. Aspelmeyer, Demonstration of an ultracold micro-optomechanical oscillator in a cryogenic cavity, Nat. Phys. **5**, 485 (2009).
[63] C. Meng, G. A. Brawley, S. Khademi, E. M. Bridge, J. S. Bennett, and W. P. Bowen, Measurement-based preparation of multimode mechanical states, Sci. Adv. **8**, eabm7585 (2022).